Intrinsic persistent spin texture in two-dimensional T-XY ($X, Y = $ P, As, Sb, Bi; $X \neq Y$)

San-Dong Guo [1,*,†] Xu-Kun Feng,[2,*] Dong Huang,[1] Shaobo Chen,[3] Guangzhao Wang,[4] and Yee Sin Ang [2]

[1]*School of Electronic Engineering, Xi'an University of Posts and Telecommunications, Xi'an 710121, China*
[2]*Science, Mathematics and Technology (SMT), Singapore University of Technology and Design (SUTD),*
8 Somapah Road, Singapore 487372, Singapore
[3]*College of Electronic and Information Engineering, Anshun University, Anshun 561000, People's Republic of China*
[4]*Key Laboratory of Extraordinary Bond Engineering and Advanced Materials Technology of Chongqing, School of Electronic Information Engineering, Yangtze Normal University, Chongqing 408100, China*

Persistent spin texture (PST) can maintain a uniform spin configuration in the momentum space, resulting in a spatially periodic mode known as a persistent spin helix (PSH). The PSH is robust against spin-independent scattering and renders an extremely long spin lifetime, which can improve the performance of potential spintronic devices. Here, T-XY ($X \neq Y = $ P, As, Sb, and Bi) monolayers with dynamical, mechanical, and thermal stabilities are predicted to intrinsically possess PST. Due to the C_{2v} point-group symmetry, a unidirectional spin configuration is preserved in the out-of-plane direction for both conduction and valence bands around the high-symmetry Γ point. That is, the expectation value of the spin S only has the out-of-plane component S_z. The application of an out-of-plane external electric field can induce in-plane components S_x and S_y, thus offering a promising platform for the on-off logical functionality of spin devices. Our work reveals an alternative family of T-phase two-dimensional (2D) materials, which could provide promising applications in spintronic devices.

I. INTRODUCTION

In a material with broken spatial inversion symmetry, the spin-orbital coupling (SOC) induces a momentum (k)-dependent spin-orbit field (SOF), which can lift spin degeneracy and leads to the nontrivial k-dependent spin textures of the spin-split bands through Rashba and Dresselhaus effects [1,2]. Practically, the strong Rashba SOC allows for electrostatic manipulation of the spin states, which has potential application for non-charge-based computing and information processing [3–5]. However, strong SOC can cause spin decoherence, which leads to the reduced spin lifetime. The impurities and defects can change the momentum of electrons in a diffusive transport regime and simultaneously randomize the spin due to the k-dependent SOF, which induces spin decoherence through the Dyakonov-Perel (DP) mechanism and limits the performance of potential spintronic devices [6].

To overcome spin dephasing, a possible way is to design a structure in which the SOF orientation is unidirectional, which can preserve a unidirectional spin configuration in the k space, known as persistent spin texture (PST). The PST will lead to a spatially periodic mode of the spin polarization, which is known as the persistent spin helix (PSH) [7,8]. The spin dephasing can be suppressed by the PSH due to SU(2) spin rotation symmetry, which renders an extremely long spin lifetime [7,9]. The PST has been demonstrated on various quantum-well heterostructures, interfaces, and surfaces [10–16]. Recently, a different approach for achieving a PST has been to impose the specific symmetry of the crystal; this approach has been realized in bulk, layered, and two-dimensional (2D) ferroelectric systems [17–27]. However, the search for 2D materials with intrinsic PST has recently received much attention due to their potential for miniaturization of spintronic devices.

Recently, similar to the α phase, the T-phase MZ ($M = $ Sn and Ge; $Z = $ S and Se) has been proposed with excellent thermal, dynamical, and mechanical stabilities, which exhibits C_{2v} symmetry and fold characteristics similar to "triple-staggered layers" [28]. These T-MX monolayers possess fine piezoelectric performance and stability [28]. Here, the T-XY ($X \neq Y = $ P, As, Sb, and Bi) monolayers are proposed with dynamical, mechanical, and thermal stabilities, which possess the same number of valence electrons as MX ($M = $ Sn and Ge; $X = $ S and Se). The T-XY monolayers are predicted to intrinsically possess PST with a unidirectional out-of-plane spin configuration (S_z) for both conduction and valence bands due to the C_{2v} point-group symmetry. When an out-of-plane external electric field is applied, the in-plane components S_x and S_y can be induced, which offers a promising platform for the on-off logical functionality of spin devices.

The rest of the paper is organized as follows. In the next section, we give our computational details and methods. In the subsequent sections, we present the crystal structure and stability, the electronic structures, and the PST of T-XY ($X \neq Y = $ P, As, Sb, and Bi) monolayers. Finally, we give our discussion and conclusion.

II. COMPUTATIONAL DETAIL

Within density functional theory (DFT) [29], the first-principles calculations are carried out by using the projector-augmented-wave (PAW) method as implemented in the

---

*These authors contributed equally to this work.
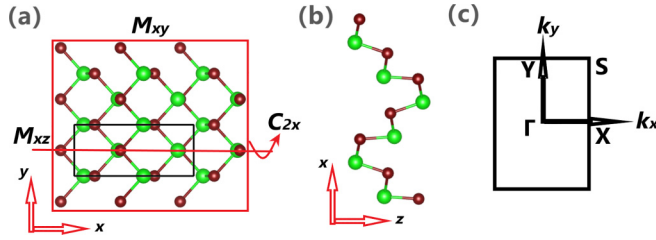†Corresponding author: sandongyuwang@163.com

FIG. 1. For T-XY ($X \neq Y$ = P, As, Sb, and Bi) monolayers, the top view (a) and the side view (b) of the crystal structure with large balls for X atoms and small balls for Y atoms are shown. The related symmetry operations are shown in panel (a). Panel (c) shows the first BZ with high-symmetry points.

Vienna *ab initio* Simulation Package (VASP) [30–32]. We use the generalized gradient approximation (GGA) of Perdew, Burke, and Ernzerhof [33] as the exchange-correlation functional. The SOC is included to investigate the electronic structures and PST of T-XY ($X \neq Y$ = P, As, Sb, and Bi) monolayers, and the details of the SOC implementation in the PAW methodology are given in Ref. [34]. The energy cutoff of 500 eV, the total energy convergence criterion of 10^{-7} eV, and the force convergence criteria of 0.001 eV Å^{-1} are set to perform the first-principles calculations. A vacuum space of more than 28 Å between slabs along the z direction is added to eliminate spurious interactions. A $3 \times 5 \times 1$ supercell is used to calculate the phonon spectrum within the finite displacement method by using the PHONOPY code [35]. The elastic stiffness (C_{ij}) is obtained by the strain-stress relationship (SSR), and the 2D C_{ij}^{2D} has been renormalized by $C_{ij}^{2D} = L_z C_{ij}^{3D}$, where L_z is the length of unit cell along the z direction. The constant energy contour plots of the spin texture are calculated by the PYPROCAR code [36]. A $9 \times 18 \times 1$ k-point mesh in the first Brillouin zone (BZ) is adopted for all calculations.

III. CRYSTAL STRUCTURE AND STABILITY

The top and side views of crystal structures of T-XY ($X \neq$ Y = P, As, Sb and Bi) monolayers are shown in Figs. 1(a) and 1(b). The primitive cell contains eight atoms, including four X atoms and four Y atoms, and each X (Y) atom is connected to three surrounding Y (X) atoms. Their optimized lattice parameters a and b along the x and y directions are listed in Table I.

The T phase has four symmetry operations: (i) identity operation E, (ii) twofold screw rotation $\bar{C}_{2x}$, (iii) glide re-
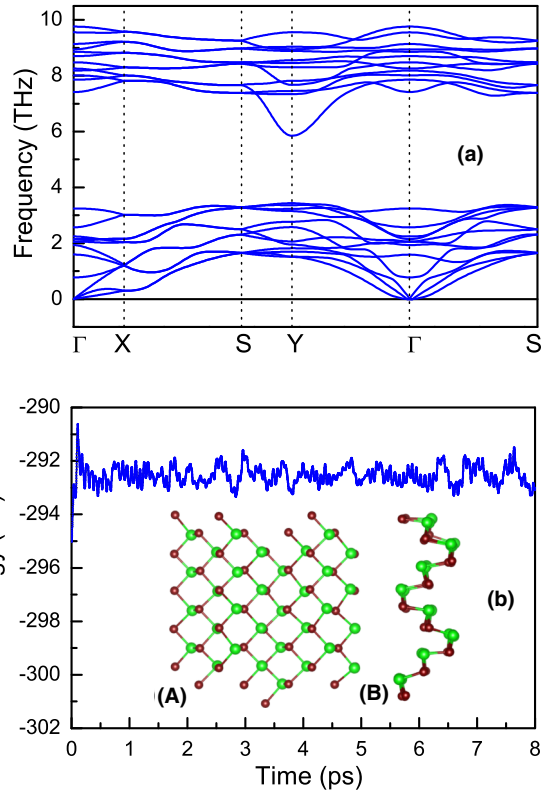

FIG. 2. For the T-SbP monolayer, (a) the phonon dispersion curves and (b) the variation of free energy during the AIMD simulation are shown. Insets show the final structures [top view (A) and side view (B)] after 8 ps at 300 K.

flection $\bar{M}_{xy}$, and (iv) reflection M_{xz} with respect to the xz plane. The $\bar{C}_{2x}$ is performed by twofold rotation around the x axis (C_{2x}), followed by translation of $\tau = (a/2, b/2)$. The $\bar{M}_{xy}$ can be obtained by reflection with respect to the xy plane followed by the translation τ. The T phase lacks inversion symmetry, allowing piezoelectric response. Because these T-XY monolayers share similar behavior, in the following, we mainly focus on the T-SbP monolayer as a representative. The results of the remaining five monolayers are briefly mentioned or shown in Figs. 1–7 [37].

To verify their dynamical stabilities, their phonon dispersions are calculated. Figure 2(a) plots the result for the monolayer SbP, which shows no imaginary frequency, indicating that the structure is dynamically stable. To investigate the

TABLE I. For the T-XY ($X \neq Y$ = P, As, Sb, and Bi) monolayer; the lattice constants a_0 and b_0 (Å); the elastic constants C_{ij} (Nm^{-1}); the Young's moduli along the x and y directions, $C_{2D}(x)$ and $C_{2D}(y)$ (Nm^{-1}); and the GGA and GGA + SOC gaps Gap and Gap^{SOC} (eV) are given.

Name	a_0	b_0	C_{11}	C_{12}	C_{22}	C_{66}	$C_{2D}(x)$	$C_{2D}(y)$	Gap	Gap^{SOC}
AsP	9.38	3.48	9.87	10.72	77.64	18.97	8.39	66.00	1.050	1.047
SbAs	9.66	3.94	7.12	11.02	55.07	13.33	4.92	38.01	0.307	0.289
SbP	8.95	3.83	3.50	9.19	60.04	17.71	2.09	35.91	0.366	0.332
BiP	8.40	4.00	4.83	3.34	54.15	17.10	4.62	51.84	0.621	0.381
BiAs	9.45	4.10	7.99	9.49	49.51	12.19	6.17	38.24	0.319	0.108
BiSb	9.94	4.35	7.49	9.94	43.04	10.64	5.19	29.85	0.354	0.026

thermal stability, the *ab initio* molecular dynamics (AIMD) simulations are performed with a $2 \times 4 \times 1$ supercell and a time step of 1 fs. Figure 2(b) shows the simulation result on the monolayer T-SbP at 300 K for 8 ps. One observes that the energy fluctuates within a small range during the whole simulation time, and the overall structure is well maintained at this temperature, indicating its good thermal stability. The linear elastic constants are calculated to determine their mechanical stabilities. Due to C_{2v} symmetry, four independent elastic constants (C_{11}, C_{12}, C_{22}, and C_{66}) can be observed, which are listed in Table I. These C_{ij} meet the Born-Huang criteria of mechanical stability ($C_{11} > 0$, $C_{66} > 0$, and $C_{11} * C_{22} > C_{12}^2$) [38], thereby verifying their mechanical stabilities. The direction-dependent Young's modulus $C_{2D}(\theta)$ can be obtained as [39]

$$C_{2D}(\theta) = \frac{C_{11}C_{22} - C_{12}^2}{C_{11}\sin^4\theta + A\sin^2\theta\cos^2\theta + C_{22}\cos^4\theta}, \quad (1)$$

where θ is the polar angle measured from x, and $A = (C_{11}C_{22} - C_{12}^2)/C_{66} - 2C_{12}$. According to Figs. 8 and 9 [37], obvious anisotropy of elasticity is observed in these T-XY monolayers. The Young's moduli of T-XY along the x and y directions are listed Table I. It is clearly seen that $C_{2D}(x)$ is much smaller than $C_{2D}(y)$. This indicates that the T-XY monolayers are more flexible and deformable along the x direction, which plays a positive effect on their piezoelectricity [28].

Although these T-XY monolayers have not been experimentally synthesized, the above calculated results show that they possess good thermal stability as well as positive dynamical and mechanical stabilities. Therefore, we expect that these monolayers can be synthesized experimentally in the future.

IV. ELECTRONIC STRUCTURES AND PERSISTENT SPIN HELIX

Figure 3 shows the energy band structures of the T-SbP monolayer calculated along high-symmetry k paths, and those of the other five monolayers are plotted in Figs. 3–7 [37]. Without including the SOC, the T-SbP, T-BiP, T-BiAs, and T-BiSb monolayers are indirect band-gap semiconductors, and the conduction band bottom (CBM) locates at Γ point, while the valence band maximum (VBM) slightly deviates from Γ along the Γ-Y path. However, the T-AsP and T-SbAs monolayers are direct band-gap semiconductors with both CBM and VBM at the Γ point. The gaps of the T-AsP, T-SbP, T-SbAs, T-BiP, T-BiAs, and T-BiSb monolayers are 1.050, 0.366, 0.307, 0.621, 0.319, and 0.354 eV, respectively. When including the SOC, the energy band structures of T-XY are modified, and they all become indirect band-gap semiconductors with both CBM and VBM slightly deviating from the Γ point. The GGA + SOC gaps of six monolayers are reduced with respect to the GGA ones. For T-XY ($X \neq Y =$ P, As, and Sb), the changes of gap are small, while the gaps of T-BiY ($Y =$ P, As, and Sb) vary greatly. The gaps of T-AsP, T-SbP, T-SbAs, T-BiP, T-BiAs, and T-BiSb become 1.047, 0.332, 0.289, 0.381, 0.108, and 0.026 eV, respectively. The related gap data are summarized in Table I. Importantly, a sizable
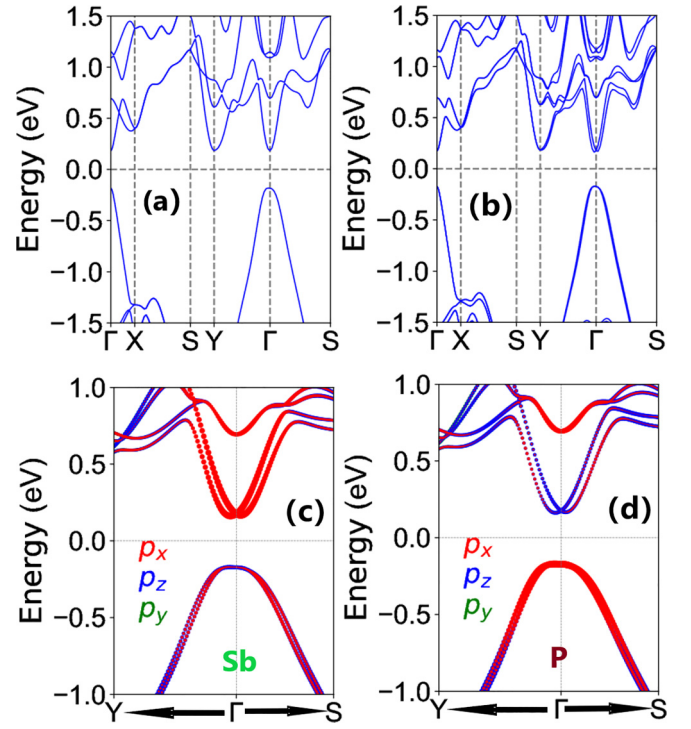

FIG. 3. For T-SbP, the energy band structures without SOC (a) and with SOC (b) are shown. Zoom-in on the energy band structures around the Γ point along the Γ-Y and Γ-S lines with projected Sb (c) and P (d) atomic p orbitals.

splitting of the bands produced by the SOC is observed. This splitting is especially pronounced around the Γ point near both the VBM and the CBM. According to Figs. 3(c) and 3(d), the Sb p_x orbitals and the P p_z orbitals contribute dominantly to the CBM, while the VBM are mainly from the contributions of the Sb p_z orbitals and the P p_x orbitals.

For the T-SbP monolayer, the top planes of Figs. 4 and 5 show the spin textures of conduction and valence bands calculated in a k_x-k_y plane centered at the Γ point with the isoenergetic surface of 0.25 and -0.25 eV, respectively. It is clearly seen that the spin polarization originates from the out-of-plane component S_z, while the in-plane components of spin (S_x and S_y) are zero. This means that the spin texture is unidirectional, which is very different from the in-plane Rashba spin textures. Such a spin texture produces a unidirectional out-of-plane SOF, resulting in a PST. The unidirectional SOF is robust against spin-independent scattering due to the PSH state, which leads to an extremely long spin lifetime by suppressing the DP spin-relaxation mechanism [6].

To explain the PST with only the out-of-plane component S_z, we establish an effective $k \cdot p$ Hamiltonian expanded at the Γ point. The twofold degeneracy at Γ corresponds to the Γ_5 double-valued irreducible representation of C_{2v}. Taking the two states as the basis vectors, the symmetry operators, C_{2x}, M_{xz}, M_{xy}, and $\mathcal{T}$ are represented in the matrix form as

$$D(C_{2x}) = -i\sigma_x, \quad D(M_{xz}) = -i\sigma_y,$$
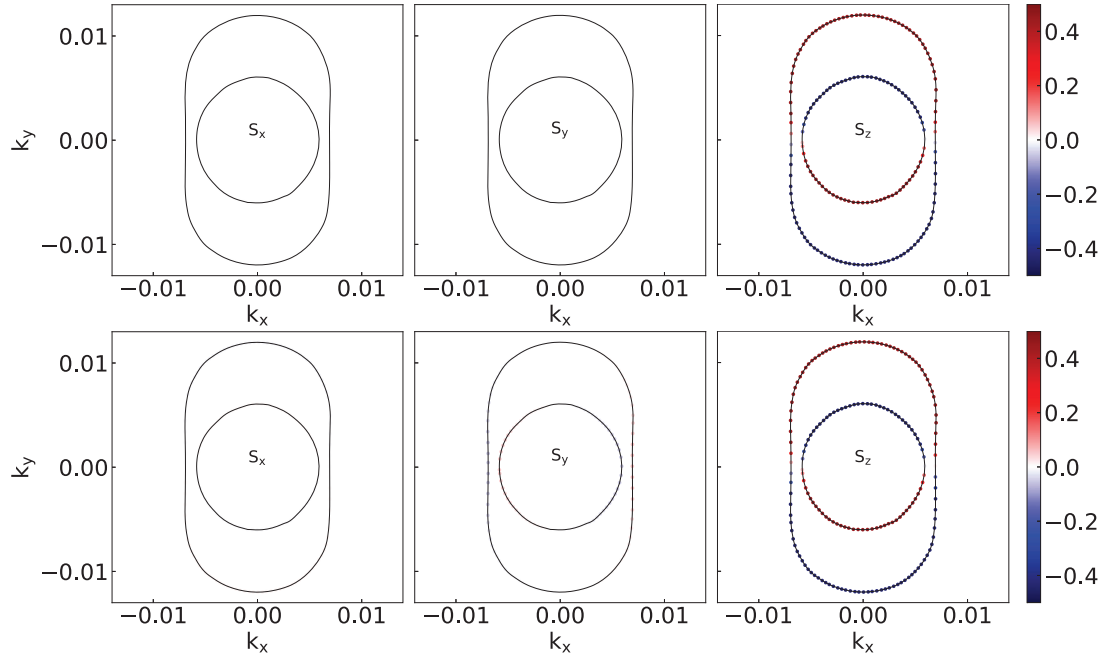$$D(M_{xy}) = -i\sigma_z, \quad D(\mathcal{T}) = -i\sigma_y\mathcal{K}, \quad (2)$$

FIG. 4. For the T-SbP monolayer, the top plane and the bottom plane show the spin texture (S_x, S_y, and S_z) calculated in a k_x-k_y plane centered at the Γ point with the isoenergetic surface of 0.25 eV above the Fermi level at $E = 0.00$ and 0.30 V/Å, respectively. The color scale shows the moduli of the spin polarization.

where $\mathcal{T}$ is the time-reversal symmetry. These symmetries constrain the Hamiltonian H by

$$C_{2x}H(\boldsymbol{k})C_{2x}^{-1} = H(k_x, -k_y),$$
$$M_{xz}H(\boldsymbol{k})M_{xz}^{-1} = H(k_x, -k_y),$$
$$M_{xy}H(\boldsymbol{k})M_{xy}^{-1} = H(k_x, k_y),$$
$$\mathcal{T}H(\boldsymbol{k})\mathcal{T}^{-1} = H(-k_x, -k_y). \tag{3}$$

We then derive the permitted terms of the effective Hamiltonian by analyzing the invariance of the possible terms under symmetry transformation. Table II shows the invariance of the 2×2 identity matrix σ_0, the Pauli matrices $\vec{\sigma}$ (σ_x, σ_y, σ_z), and the wave vector $\vec{k}$ (k_x, k_y) under the symmetry operators. After an item-by-item analysis of the k^0, k^1, k^2, and k^3 orders, as shown in Table III, we obtain that σ_0, $k_x^2\sigma_0$, $k_y^2\sigma_0$, $k_y\sigma_z$, $k_x^2k_y\sigma_z$, and $k_y^3\sigma_z$ are invariant terms under the symmetry operations.
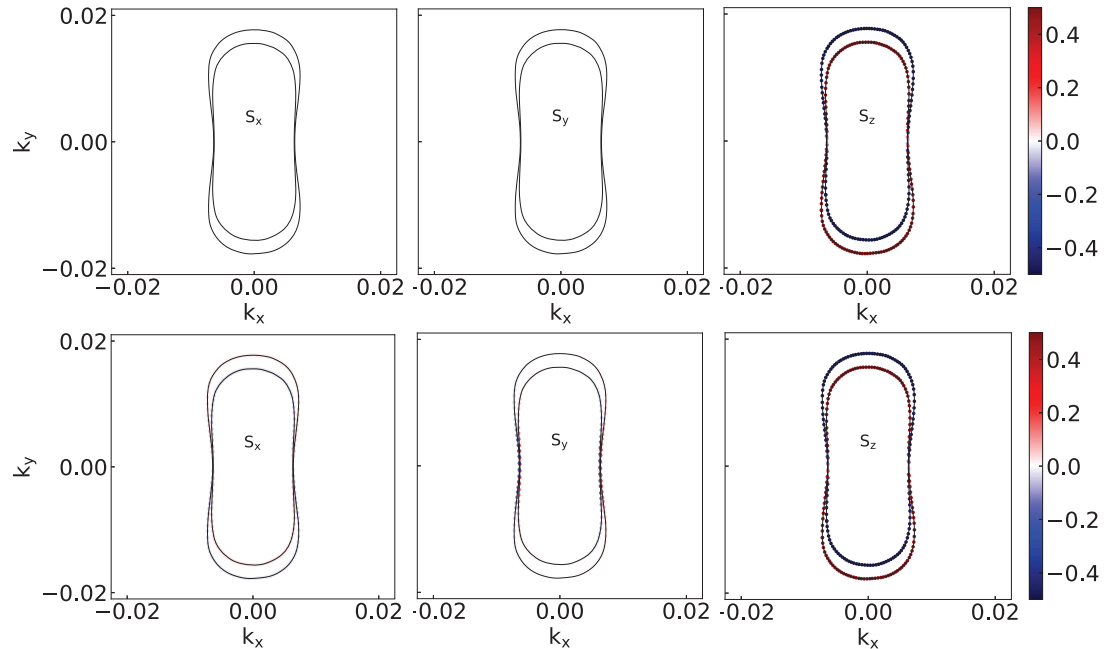
FIG. 5. For the T-SbP monolayer, the top plane and the bottom plane show the spin texture (S_x, S_y, and S_z) calculated in a k_x-k_y plane centered at the Γ point with the isoenergetic surface of -0.25 eV below the Fermi level at $E = 0.00$ and 0.30 V/Å, respectively. The color scale shows the moduli of the spin polarization.

TABLE II. The invariance of the 2×2 identity matrix σ_0, Pauli matrices $\vec{\sigma}$ (σ_x, σ_y, σ_z), and the wave vector $\vec{k}$ (k_x, k_y) under symmetry operators. "+" represents the term is invariant under symmetry operations, while "-" means the term becomes the opposite.

Terms	C_{2x}	M_{xz}	M_{xy}	$\mathcal{T}$
σ_0	+	+	+	+
σ_x	+	-	-	-
σ_y	-	+	-	-
σ_z	-	-	+	-
k_x	+	+	+	-
k_y	-	-	+	-

Hence, the $k \cdot p$ effective Hamiltonian can be written as

$$H(k) = \left(c_0 + c_1 k_x^2 + c_2 k_y^2\right)\sigma_0 + \left(c_3 k_y + c_4 k_x^2 k_y + c_5 k_y^3\right)\sigma_z, \tag{4}$$

where c_i are model parameters. We utilize this model to fit the DFT band around the Γ point for the conduction band of T-SbP, as displayed in Fig. 10 [37]. The values of the fitting parameters are $c_0 = 0.176$ eV, $c_1 = 4.661$ eV Å^2, $c_2 = 27.552$ eV Å^2, $c_3 = -1.141$ eV Å, $c_4 = 106.987$ eV Å^3, and $c_5 = -46.937$ eV Å^3. Since the spin operator S_z commutes with the Hamiltonian equation (4), the spin operator S_z is a conserved quantity. The expectation value of the spin S only has the out-of-plane component, which produces the unidirectional out-of-plane spin configuration in k space.

On the other hand, by ignoring the high-order k items, the linear-term parameter α, through the relation $\alpha = c_3 = 2E_R/k_0$, can be obtained, where E_R and k_0 are the shifting energy and the wave vector along the y direction. The formation of the PSH mode should have a substantially small charac-

TABLE III. The invariance of the possible terms up to k^3 order under symmetry operators. "+" represents the term is invariant under symmetry operations, while "-" means the term becomes the opposite.

Terms	C_{2x}	M_{xz}	M_{xy}	$\mathcal{T}$
$\sigma_0, k_x^2\sigma_0, k_y^2\sigma_0$	+	+	+	+
$\sigma_x, k_x^2\sigma_x, k_y^2\sigma_x$	+	-	-	-
$\sigma_y, k_x^2\sigma_y, k_y^2\sigma_y$	-	+	-	-
$\sigma_z, k_x^2\sigma_z, k_y^2\sigma_z$	-	-	+	-
$k_x\sigma_0, k_x^3\sigma_0, k_xk_y^2\sigma_0$	+	+	+	-
$k_x\sigma_x, k_x^3\sigma_x, k_xk_y^2\sigma_x$	+	-	-	+
$k_x\sigma_y, k_x^3\sigma_y, k_xk_y^2\sigma_y$	-	+	-	+
$k_x\sigma_z, k_x^3\sigma_z, k_xk_y^2\sigma_z$	-	-	+	+
$k_y\sigma_0, k_y^3\sigma_0, k_x^2k_y\sigma_0$	-	-	+	-
$k_y\sigma_x, k_y^3\sigma_x, k_x^2k_y\sigma_x$	-	+	-	+
$k_y\sigma_y, k_y^3\sigma_y, k_x^2k_y\sigma_y$	+	-	-	+
$k_y\sigma_z, k_y^3\sigma_z, k_x^2k_y\sigma_z$	+	+	+	+
$k_xk_y\sigma_0$	-	-	+	+
$k_xk_y\sigma_x$	-	+	-	-
$k_xk_y\sigma_y$	+	-	-	-
$k_xk_y\sigma_z$	+	+	+	-

TABLE IV. For several selected 2D PST systems [T-XY ($X \neq Y = $ P, As, Sb, and Bi), MN ($M = $ Sn and Ge; $N = $ S, Se, and Te) and GaMN ($M = $ Se and Te; $N = $ Cl, Br, and I)], the spin-splitting parameter α (eV · Å), the effective mass m^* (m_0), and the characteristic spin rotation length λ (nm).

Monolayer	α	m^*	λ	Reference
AsP	0.059	0.120	67.675	This work
SbAs	0.454	0.092	11.471	This work
SbP	1.103	0.116	3.745	This work
BiP	2.454	0.094	2.077	This work
BiAs	4.359	0.067	1.640	This work
BiSb	7.113	0.056	1.203	This work
MN	$0.07 \sim 1.67$		$1.82 \sim 890$	Ref. [25]
GaMN	$0.53 \sim 2.65$		$1.20 \sim 6.57$	Ref. [21]

teristic spin rotation length λ. Here, the characteristic spin rotation length λ can be estimated by using $\lambda = \pi \hbar^2/\alpha m^*$, where m^* is the electron effective mass (Here, we only consider the conduction bands due to large spin-splitting.). The electron effective mass m^* is evaluated from the band dispersion along the Γ-Y line in the CBM. For several selected 2D PST systems, the spin-splitting parameter α, the effective mass m^*, and the characteristic spin rotation length λ are summarized in Table IV. The α values of T-SbP, T-BiP, T-BiAs, and T-BiSb are comparable with those reported for several 2D PST systems, and the small characteristic spin rotation length λ of the PSH mode is typically on the scale of the lithographic dimension used in the recent semiconductor industry. Thus, the T-SbP, T-BiP, T-BiAs, and T-BiSb monolayers should be promising for miniaturization of spintronic devices.

The application of the external electric field can modify the spin texture of T-SbP. So, an external out-of-plane electric field E is applied, which breaks both the C_{2x} rotational and the M_{xy} in-plane mirror symmetries. The gap of T-SbP as a function of E is plotted in Fig. 6, and the related energy band structures are shown in Fig. 11 [37]. It is clearly seen that the gap basically remains unchanged when E is less than about 0.34 V/Å. At about $E = 0.38$ V/Å, a semiconductor-to-metal phase transition can be observed.

Under the out-of-plane external electric field, the effective Rashba contribution should be added in the Hamiltonian
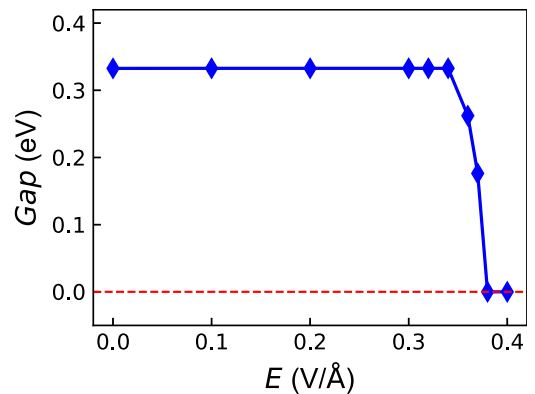

FIG. 6. For the T-SbP monolayer, the energy band gap as a function of out-of-plane external electric field E is shown.
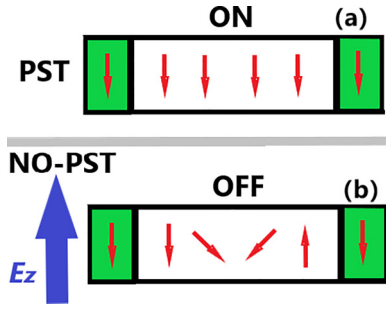
FIG. 7. Schematic of spintronic devices: the red arrows represent spin, while the blue arrow represents the out-of-plane electric field.

equation (4), which has the isotropic form [1]

$$H_R^{\text{iso}} = \alpha_R^{\text{iso}}(k_x\sigma_y - k_y\sigma_x). \quad (5)$$

The introducing Rashba term will induce the in-plane spin components due to the broken in-plane mirror symmetry M_{xy} caused by the out-of-plane external electric field. To confirm this, the bottom planes of Figs. 4 and 5 show the spin textures of conduction and valence bands calculated in a k_x-k_y plane centered at the Γ point with the isoenergetic surface of 0.25 and -0.25 eV for T-SbP at $E = 0.30$ V/Å. It is clearly observed that significant in-plane spin components (S_x and S_y) are induced, thus breaking the PST and perturbing the PSH state.

The in-plane spin components can be turned on by an applied out-of-plane electric field, which provides a possibility of the on-off logical functionality of spin devices by controlling the passage of electrons (see Fig. 7). For example, two ferromagnetic electrodes in the same direction are set for source and drain electrodes. Without the out-of-plane electric field, the out-of-plane orientation of the spin polarization injected from the source electrode is maintained due to PST, when the injected electrons pass through the T-SbP channel [Fig. 7(a)]. When the external electric field is applied, the PST is broken, and the PSH state is perturbed. The spin of electrons in the channel will rotate and will be blocked by the drain electrode [Figure 7(b)]. The function of the spintronic switch can be realized in the possible spintronic device.

The PST can maintain a uniform spin configuration in the momentum space, which supports an extraordinarily long spin lifetime of carriers. In a more realistic system, the DP processes can be strongly enhanced due to the cubic (k^3) terms of the SOC, which are frequently ignored, and then the PSH decays [40]. However, the spin operator S_z commutes with the Hamiltonian equation (4), which includes both k-linear and k^3 terms. So, the spin operator S_z is a conserved quantity, which cannot be affected by the cubic terms of the SOC. Even in quantum wells with a perfectly symmetric environment, a random Rashba field can be induced due to fluctuations of the concentration of dopant ions [41], which has been confirmed in GaAs (110) quantum wells [42]. Therefore, a possible mechanism which makes the PSH decay in our proposed systems is a random Rashba coupling.

V. DISCUSSION AND CONCLUSION

The conventional SOC Hamiltonian in a 2D electron gas can be written as [43]

$$H_{\text{SOC}} = \sum_j \alpha_j(\vec{h}_{[j]} \cdot \vec{\sigma})k_j, \quad (6)$$

where α_j is the corresponding SOC constant for a given component of momentum, and $\vec{h}_{[j]}$ is a unit-length vector. The interaction H_{SOC} is produced in a 2D electron gas from various sources. The piezotronic effect on Rashba SOC in a ZnO/P3HT nanowire array structure has been investigated experimentally [44]. It has been found that the Rashba SOC can be effectively tuned by the inner-crystal piezopotential created inside the ZnO nanowires instead of by an externally applied voltage.

Due to broken spatial inversion symmetry, the piezoelectric response along the x direction can be observed with a uniaxial in-plane strain, which can tune spin-splitting of T-SbP. When a uniaxial in-plane vibration is applied to T-SbP, the spin-splitting will be modulated periodically. As shown in Fig. 12(a) of Ref. [37], the compressive strain produces a negative electric field and then reduces the spin-splitting of PST. However, Fig. 12(b) of Ref. [37] shows that the tensile strain induces a positive electric field and then enhances the spin-splitting of PST. So, the orthorhombic primitive cell is used to calculate the piezoelectric stress coefficients e_{ij} of T-XY ($X \neq Y =$ P, As, Sb, and Bi), and then the piezoelectric strain coefficients d_{ij} are obtained by C_{ij} and e_{ij} [28]. The related data are listed in Table I [37]. The $|d_{11}|$ of T-SbP is as high as 266.15 pm/V, which plays a positive effect on tuning spin-splitting by the piezoelectric effect. So, the spin-splitting of PST in T-XY ($X \neq Y =$ P, As, Sb, and Bi) can be tuned by the piezoelectric effect.

In summary, based on the first-principles calculations along with symmetry analysis, we have systematically investigated the electronic properties of 2D T-XY ($X \neq Y =$ P, As and Sb) monolayers with dynamical, mechanical, and thermal stabilities. Because of C_{2v} point-group symmetry, the unidirectional out-of-plane spin configurations are preserved in 2D T-XY ($X \neq Y =$ P, As, and Sb) monolayers, giving rise to the PST. It is found that the PST is observed near both the VBM and the CBM around the Γ point. The out-of-plane electric field can be used to perturb the PST, which provides the possibility to realize an electronic device for the switching function. Our works reveal an alternative 2D family of materials that have great potential for spintronic device applications.

[1] E. I. Rashba, Sov. Phys. Solid State **2**, 1109 (1960).

[2] G. Dresselhaus, Phys. Rev. **100**, 580 (1955).

[3] J. Nitta, T. Akazaki, H. Takayanagi, and T. Enoki, Phys. Rev. Lett. **78**, 1335 (1997).

[4] A. Manchon, H. C. Koo, J. Nitta, S. M. Frolov, and R. A. Duine, Nat. Mater. **14**, 871 (2015).

[5] P. Chuang, S. H. Ho, L. W. Smith *et al.*, Nat. Nanotechnol. **10**, 35 (2015).

[6] M. I. Dyakonov and V. I. Perel, Sov. Phys. Solid State **13**, 3023 (1972).

[7] B. A. Bernevig, J. Orenstein, and S.-C. Zhang, Phys. Rev. Lett. **97**, 236601 (2006).

[8] J. Schliemann, Rev. Mod. Phys. **89**, 011001 (2017).

[9] P. Altmann, M. P. Walser, C. Reichl, W. Wegscheider, and G. Salis, Phys. Rev. B **90**, 201306(R) (2014).

[10] J. D. Koralek, C. P. Weber, J. Orenstein, B. A. Bernevig, S.-C. Zhang, S. Mack, and D. D. Awschalom, Nature (London) **458**, 610 (2009).

[11] M. P. Walser, C. Reichl, W. Wegscheider, and G. Salis, Nat. Phys. **8**, 757 (2012).

[12] J. Ishihara, Y. Ohno, and H. Ohno, Appl. Phys. Express **7**, 013001 (2014).

[13] M. Kohda, V. Lechner, Y. Kunihashi *et al.*, Phys. Rev. B **86**, 081306(R) (2012).

[14] A. Sasaki, S. Nonaka, Y. Kunihashi, M. Kohda, T. Bauernfeind, T. Dollinger, K. Richter, and J. Nitta, Nat. Nanotechnol. **9**, 703 (2014).

[15] N. Yamaguchi and F. Ishii, Appl. Phys. Express **10**, 123003 (2017).

[16] M. A. U. Absor, F. Ishii, H. Kotaka, and M. Saito, Appl. Phys. Express **8**, 073006 (2015).

[17] L. L. Tao and E. Y. Tsymbal, Nat. Commun. **9**, 2763 (2018).

[18] C. Autieri, P. Barone, J. Slawińska, and S. Picozzi, Phys. Rev. Mater. **3**, 084416 (2019).

[19] H. Djani, A. C. Garcia-Castro, W. Y. Tong, P. Barone, E. Bousquet, S. Picozzi, and P. Ghosez, npj Quantum Mater. **4**, 51 (2019).

[20] H. Ai, X. Ma, X. Shao, W. Li, and M. Zhao, Phys. Rev. Mater. **3**, 054407 (2019).

[21] S. A. Sasmito, M. Anshory, I. Jihad, and M. A. U. Absor, Phys. Rev. B **104**, 115145 (2021).

[22] M. A. U. Absor and F. Ishii, Phys. Rev. B **103**, 045119 (2021).

[23] F. Jia, S. Hu, S. Xu, H. Gao, G. Zhao, P. Barone, A. Stroppa, and W. Ren, J. Phys. Chem. Lett. **11**, 5177 (2020).

[24] M. A. U. Absor and F. Ishii, Phys. Rev. B **99**, 075136 (2019).

[25] M. A. U. Absor and F. Ishii, Phys. Rev. B **100**, 115104 (2019).

[26] H. Lee, J. Im, and H. Jin, Appl. Phys. Lett. **116**, 022411 (2020).

[27] H. J. Zhao, H. Nakamura, R. Arras, C. Paillard, P. Chen, J. Gosteau, X. Li, Y. Yang, and L. Bellaiche, Phys. Rev. Lett. **125**, 216405 (2020).

[28] H. Lei, T. Ouyang, C. Y. He, J. Li, and C. Tang, Appl. Phys. Lett. **122**, 062903 (2023).

[29] P. Hohenberg and W. Kohn, Phys. Rev. **136**, B864 (1964); W. Kohn and L. J. Sham, **140**, A1133 (1965).

[30] G. Kresse, J. Non-Cryst. Solids **192-193**, 222 (1995).

[31] G. Kresse and J. Furthmüller, Comput. Mater. Sci. **6**, 15 (1996).

[32] G. Kresse and D. Joubert, Phys. Rev. B **59**, 1758 (1999).

[33] J. P. Perdew, K. Burke, and M. Ernzerhof, Phys. Rev. Lett. **77**, 3865 (1996).

[34] S. Steiner, S. Khmelevskyi, M. Marsmann, and G. Kresse, Phys. Rev. B **93**, 224425 (2016).

[35] A. Togo, F. Oba, and I. Tanaka, Phys. Rev. B **78**, 134106 (2008).

[36] U. Herath, P. Tavadze, X. He, E. Bousquet, S. Singh, F. Munoz, and A. H. Romero, Comput. Phys. Commun. **251**, 107080 (2020).

[37] See Supplemental Material at http://link.aps.org/supplemental/10.1103/PhysRevB.108.075421 for the phonon band dispersions, AIMD results, and energy band structures of T-AsP, T-SbAs, T-BiP, T-BiAs, and T-BiSb; the direction-dependent Young's moduli $C_{2D}(\theta)$ and piezoelectric coefficients e_{ij}/d_{ij} of T-XY ($X \neq Y =$ P, As, Sb, and Bi); the energy band structures of T-SbP as a function of the electric field E; and the schematic of strain-tuned persistent spin-splitting.

[38] M. Born and K. Huang, Am. J. Phys. **23**, 474 (1955).

[39] E. Cadelano, P. L. Palla, S. Giordano, and L. Colombo, Phys. Rev. B **82**, 235414 (2010).

[40] M. Prada and D. Pfannkuche, Phys. Rev. B **95**, 045421 (2017).

[41] E. Ya. Sherman, Appl. Phys. Lett. **82**, 209 (2003).

[42] G. M. Müller, M. Römer, D. Schuh, W. Wegscheider, J. Hübner, and M. Oestreich, Phys. Rev. Lett. **101**, 206601 (2008).

[43] I. V. Tokatly and E. Ya. Sherman, Ann. Phys. **325**, 1104 (2010).

[44] L. Zhu, Y. Zhang, P. Lin *et al.*, ACS Nano **12**, 1811 (2018).